

Machine learning quantum field theory with local probes

Daniel Grimmer,^{1,2,*} Irene Melgarejo-Lermas,^{1,3,†} and Eduardo Martín-Martínez^{1,3,4,‡}

¹*Institute for Quantum Computing, University of Waterloo, Waterloo, ON, N2L 3G1, Canada*

²*Dept. Physics and Astronomy, University of Waterloo, Waterloo, ON, N2L 3G1, Canada*

³*Dept. Applied Math., University of Waterloo, Waterloo, ON, N2L 3G1, Canada*

⁴*Perimeter Institute for Theoretical Physics, Waterloo, ON, N2L 2Y5, Canada*

We propose the use of machine learning techniques to address the problem of local measurements in quantum field theory. In particular we discuss how neural networks can efficiently process measurement outcomes from local probes to determine both local and non-local features of the quantum field. As toy examples we show: a) how a particle detector distinguishes boundary conditions imposed on the field without the need of signals propagating from them, and b) how detectors can determine the temperature of the quantum field without thermalizing with it. We discuss how the formalism proposed can be used for any kind of local measurement on a quantum field and, by extension, to local measurements of non-local features in many-body quantum systems.

Introduction.- Our current understanding of the fundamental nature of matter comes from quantum field theory (QFT). However, the process of obtaining experimental information from QFTs is arguably a difficult task to formalize. For example, projective measurements in QFT are incompatible with its relativistic nature: they cannot be localized [1], they can introduce ill-defined operations [2] and enable superluminal signaling even in simple setups [3]. For these reasons, it has been strongly argued that projective measurements should be rejected in any relativistic field theory [3–5]. Nevertheless, from experiments at the LHC to the role of the retina in human sight, quantum fields are subject to measurements where data is extracted through their interaction with localized probes. Such probes (e.g., atoms for the electromagnetic field) can be generally modeled by particle detectors [6]. Particle detectors allow us to perform indirect measurements on the field that are well-defined [7] and physically meaningful [8].

Given the result of local measurements, how much information can one recover about the field? It is thinkable that with a sufficient number of carefully chosen measurements on an array of probes coupling to the field long enough, one should be able to determine everything about the field, at least in principle. We say ‘in principle’ because there is usually no direct translation between 1) the theoretical predictions of particle detectors in two different scenarios (usually transition probabilities [9–14]), and 2) the actual experimental data obtained when measuring a field locally in those scenarios. The probes we use to measure quantum fields are usually simple in nature, and certainly much simpler and with smaller Hilbert spaces than the QFT itself. Because of this, translating measurement data (e.g., a large set of zeros and ones generated by measuring a two-dimensional particle detector) into concrete claims about the field seems, a priori, a very complicated task.

However we will see that one does not need complicated protocols to learn about global features of the field. As we will show, a simple measurement protocol on a single probe coupling for short times is enough. This is because a thermalized quantum field stores information about its global structure locally, albeit in a very scrambled way [15–20]. To extract and unscramble this information we propose the use of machine learning. In recent years, machine learning has proven effective at processing data from quantum systems [21–29]. By training a neural network to translate probe measurement data into features of a QFT we will show that local probes can read non-local information about the field. For instance, local probes can learn about far boundary conditions even before a signal has time to propagate between them. Also, local probes can learn the KMS temperature of the field with great accuracy even before they have time to thermalize with it. This shows that combining machine learning with the usual detector model tools used in QFT we can overcome the complexity difficulties in translating outcomes of local measurements into concrete claims on the abstract features of the QFTs.

Although we will consider a simple toy model, the setup that we present illustrates how one can translate the outcome of very general local measurements to concrete, physical statements about global features of a quantum field (e.g., its temperature, entanglement structure, boundary conditions, space-time geometry, topology etc.), without having to think very much about what local measurements are optimal. We put the burden of the ‘translation job’ not in the experimental design, but in the data processing, in a way that can adapt to any practical experimental protocol.

A simple model.- As a proof-of-principle we study a 1+1 dimensional scalar field coupled locally to a harmonic oscillator probe [30–36]. The free Hamiltonian of the field-probe system is $\hat{\mathcal{H}}_\phi + \hat{\mathcal{H}}_D$ with $\hat{\mathcal{H}}_D = \hbar\omega_D(\hat{p}_D^2 + \hat{q}_D^2)/2$ (where \hat{q}_D and \hat{p}_D are the probe’s quadrature operators satisfying

* dgrimmer@uwaterloo.ca

† i2melgar@uwaterloo.ca

‡ emartinmartinez@uwaterloo.ca

$[\hat{q}_D, \hat{p}_D] = i\hbar\mathbb{1}$, and

$$\hat{\mathcal{H}}_\phi = \frac{1}{2} \int_{-\infty}^{\infty} dx \, c^2 \hat{\pi}(x)^2 + (\partial_x \hat{\phi}(x))^2 + \frac{m^2 c^2}{\hbar^2} \hat{\phi}(x)^2, \quad (1)$$

where $x := (t, x)$ and where $\hat{\phi}(x)$ and $\hat{\pi}(x)$ are the field observables satisfying the canonical commutation relations $[\hat{\phi}(t, x), \hat{\pi}(t, y)] = i\hbar\delta(x - y)\mathbb{1}$. The probe couples locally to the field via an interaction Hamiltonian

$$\hat{\mathcal{H}}_{\text{INT}} = \lambda \chi(t) \int_{-\infty}^{\infty} dx \, F(x) \hat{q}_D \otimes \hat{\phi}(x). \quad (2)$$

$\chi(t)$ is a switching function and $F(x)$ is the probe's smearing function (with units inverse length). From (2) we can read that the probe only 'sees' the field in the support of $F(x)$. This coupling is motivated by the Unruh-DeWitt model [37, 38], which captures all the fundamental features of the light-matter interaction [6, 39].

Although it is not necessary for our methods to work, we consider a UV-cutoff by discretizing space in a standard way [40, 41]. This UV-cutoff is motivated by the lengthscale of the probe's smearing function: If the support of $F(x)$ has a lengthscale σ , the probe does not couple to field modes with wavenumber $|k| \gg \sigma^{-1}$. The coupling to these modes is suppressed in the interaction Hamiltonian as the tails of the Fourier transform of $F(x)$ [42] (for the interested reader we provide some discussion in the appendix A). In particular, we take the probe to have a Gaussian smearing with standard deviation σ . This motivates the choice of cutoff $|k| \leq K := 7/\sigma$. Doing this yields the following field and interaction Hamiltonians,

$$\hat{\mathcal{H}}_\phi^{\text{UV}} = \sum_n \frac{m c^2}{2} (\hat{p}_n^2 + \hat{q}_n^2) + \frac{\hbar^2}{2m a^2} (\hat{q}_{n+1} - \hat{q}_n)^2, \quad (3)$$

$$\hat{\mathcal{H}}_{\text{INT}}^{\text{UV}} = \lambda_0 \chi(t) \sum_n a F(x_n) \hat{q}_D \otimes \hat{q}_n, \quad (4)$$

where $a = \pi/K$ is the spacing of the lattice $x_n := (t, n a)$ and we have defined dimensionless field operators $\hat{q}_n := \sqrt{am/\hbar^2} \hat{\phi}(x_n)$ and $\hat{p}_n := \sqrt{a/m} \hat{\pi}(x_n)$ which satisfy $[\hat{q}_i, \hat{p}_j] = i\delta_{ij}\mathbb{1}$. $\lambda_0 = \lambda \hbar/\sqrt{am}$ is the energy scale of the probe-field coupling. We can further impose an IR-cutoff introducing boundary conditions which restrict the field to a region $x \in [0, L]$ where $L = N a$ (i.e., field in a cavity). We note that the discretization has established a parallel between the QFT problem and a many-body problem, thus the techniques discussed in this letter apply equally well to many-body systems considered generally.

Boundary Conditions and Thermometry. - To simulate a change of boundary condition, we will modify the coupling, \hat{H}_{last} , of the lattice to the spatial mode farthest from the probe. We summarize the modified couplings that we consider in Table I.

In the first two cases, we modify the strength of \hat{H}_{last} . In the third case (signaling) we consider a time-dependent coupling which turns on suddenly at $t = 0$.

y-label	Name	\hat{H}_{last} for $t < 0$	\hat{H}_{last} for $t \geq 0$
y=1	Full Bond	$g \hat{q}_{N-1} \otimes \hat{q}_N$	Same as $t < 0$
y=2	Cut Bond	$0 \hat{q}_{N-1} \otimes \hat{q}_N$	Same as $t < 0$
y=3	Signal	$0 \hat{q}_{N-1} \otimes \hat{q}_N$	$g \hat{q}_{N-1} \otimes \hat{q}_N$

TABLE I. Modifications to the coupling, \hat{H}_{last} , connecting the last spatial mode to the rest of the lattice. $g = \hbar^2/ma^2$.

In all cases we assume that the field has thermalized to the ground state of its $t < 0$ Hamiltonian well before $t = 0$. In the signaling case we take the last spatial mode to be in an excited state so that its coupling at $t = 0$ significantly disturbs the field, sending a noticeable signal. In particular, we choose a strongly squeezed state (squeezing of 8 dB).

Note that comparing cases 2 and 3 will allow us to explicitly measure the signal-propagation speed on the lattice. In both cases the field (neglecting the last spatial mode) is in exactly the same state prior to $t = 0$. In case 3, the field is disturbed locally by the sudden coupling of the last spatial mode. This disturbance will then propagate and eventually arrive at our probe system. Thus we can define the effective signaling time as the time it takes the probe to differentiate between cases 2 and 3. Importantly, if the probe is able to differentiate cases 1 and 2 in less than this effective signaling time it can not be due to having received a signal from the boundary.

We will also evaluate the probe's ability to distinguish quantum fields with different temperatures via short-time measurements. We will show, perhaps against intuition, that probes acquire enough information to figure out the temperature of the quantum field before they have time to thermalize.

Data generation, processing and training - We now show how we generate data from the local probe, and how we preprocess that data for the neural network to train on. We consider the following measurement procedure:

1. Initialize the probe to its ground state and couple it locally to the field beginning at time $t = 0$ (i.e., $\chi(t)$ is a step function).
2. At time $t_m = T_{\text{MIN}}$, perform a projective measurement of the probe's \hat{q}_D quadrature and record the result.
3. Repeat steps 1 – 2 but measure \hat{p}_D , then repeat steps 1 – 2 but measure $\hat{r}_D = (\hat{q}_D + \hat{p}_D)/\sqrt{2}$.
4. Repeat steps 1 – 3, $N_{\text{TIMES}} - 1$ more times increasing the measurement time, t_m , by Δt each time.
5. Repeat this whole process N_{TOM} times.

Applying this measurement procedure yields raw data $\mathbf{x}_{\text{raw}} \in \mathbb{R}^{N_M}$, where $N_M = 3 \times N_{\text{TIMES}} \times N_{\text{TOM}}$, to which we can associate a label, y , depending on the boundary condition (or temperature). We could train our neural

network directly on this labeled data, however, to speed up training, we first compress and process the data.

Although our techniques work outside the Gaussian case, in our toy examples the field and probe are both initially in Gaussian states (squeezed, vacuum, thermal), and since all of our Hamiltonians are quadratic in quadrature operators, our probe will remain in a Gaussian state throughout its interaction with the field [43]. Thus the values in \mathbf{x}_{raw} are normally distributed. For instance, each of our N_{TOT} measurement, q_k , of \hat{q}_D at a time t will be distributed as $q_k \sim \mathcal{N}(\langle \hat{q}_D \rangle, \sigma_{qq})$, where $\mathcal{N}(\mu, \sigma^2)$ is the normal distribution with mean μ and variance σ^2 , and $\langle \hat{q}_D \rangle = \langle \hat{q}_D(t) \rangle$ and $\sigma_{qq} = \langle \hat{q}_D^2(t) \rangle - \langle \hat{q}_D(t) \rangle^2$. We can efficiently compute $\langle \hat{q}_D \rangle$ and σ_{qq} as well as all the other parameters determining the distribution of our data.

The sample mean, $\bar{q}(t) = \sum_{k=1}^{N_{\text{TOT}}} q_k / N_{\text{TOT}}$, and sample variance, $\bar{s}_q^2(t) = \sum_{k=1}^{N_{\text{TOT}}} (q_k - \bar{q}(t))^2 / (N_{\text{TOT}} - 1)$, are sufficient statistics for independent identically distributed normal data [44]. Note that the above holds for our measurements of \hat{q}_D , \hat{r}_D and \hat{p}_D at each time. Thus we can losslessly compress our data to N_{TIMES} sextuplets of the form $\{\bar{q}(t), \bar{r}(t), \bar{p}(t), \bar{s}_q^2(t), \bar{s}_r^2(t), \bar{s}_p^2(t)\}$. Thus in total, our compressed data can be represented by a vector $\mathbf{x} \in \mathbb{R}^d$ where $d = 6N_{\text{TIMES}}$. We can collect n instances of this data into a $d \times n$ design matrix $\mathbf{X} = (\mathbf{x}_1, \dots, \mathbf{x}_n)^\top$ and a vector of labels $\mathbf{y} = (y_1, \dots, y_n)^\top$. This design matrix is then divided into training data ($n_{\text{train}} = 0.75n$) for training the neural network, and validation data ($n_{\text{valid}} = 0.25n$) for testing the accuracy of the trained network. The network is not exposed to any of the validation data during training. We then perform standard preprocessing [45] on the compressed data to prepare it for training the neural network: we center the data, do principal component analysis, and whiten the data.

Let us summarize the training process. Neural networks model complex high dimensional function by alternatively applying tunable linear-affine transformations and fixed non-linear transformations to their inputs. The parameters controlling the linear-affine transformations (weights and biases) are then adjusted through training to minimize some cost function. The network architecture and training procedure that we use are standard [45]. For the curious reader, we include our code [46] and a summary of our preprocessing, network architecture and training process in appendix B.

Remote Boundary Sensing.- We consider a detector roughly of atomic size, for simplicity with Gaussian smearing function of width, $\sigma = 53$ pm. Taking the UV-cutoff at $K = 7/\sigma$ gives us a lattice spacing of $a = \pi/K = 23.7$ pm. We take the boundary to be at a distance $L = 200a = 90\sigma = 4.7$ nm. We take the detector to have an excitation energy $\hbar\omega_D = 130$ eV and the field to have a mass $mc^2 = 1$ eV. Note that in this example the field is approximately massless, since its mass is more than a hundred times smaller than any other energy scale in the problem. Finally we investigate the strong coupling regime (which is non-perturbative), where the energy scale of the probe-field coupling is near

the probe's free energy scale, $\lambda_0 = \hbar\omega_D = 130$ eV. Note that the choice of parameters is just for demonstration purposes, similar were also obtained for a large set of different parameters.

The results are plotted in Fig 1. We plot the actual performance of the neural network (solid line) and lower and upper bounds to the optimal theoretical accuracy (dashed lines) based on the Hellinger distance (see the appendix C for details). The green triangle lines show the causal behaviour of the setup: when we send a signal from the further boundary to the detector (by coupling a new oscillator at $t = 0$) the neural network accuracy and Hellinger bounds both indicate that it is impossible to tell if a signal was sent in less than ≈ 14.6 as. Compare this to the signal-to-edge-of-detector light-crossing time $(L - 6\sigma)/c = 14.6$ as (vertical red line in Fig 1). Indeed our toy model is very approximately relativistically causal, as a good quantum field theory on the lattice should be.

The blue circle lines represent the ability for the neural network to tell, based on the processing of local detector measurements, the kind of boundary condition at the far end of the lattice. Here, the information about the boundary has had time to spread all over space in the thermalization process: the ground state knows locally about its boundary conditions [11, 13]. Indeed, the network accuracy and Hellinger bounds both show that the nature of the field boundary can be resolved long before any signal propagates to the detector. This allows the probe to see the boundary ‘without light’, that is, in the vacuum state of the theory and much before the light-crossing time of the lattice. Notice that a) the neural network behaves optimally (tracks the bounds) and b) the network can accurately distinguish the two boundary conditions by considering a number of measurements that is still relatively small as compared with the typical number of atoms in a macroscopic sensor, $N_{\text{TOT}} = 10^{20} \ll N_A \approx 10^{24}$.

Thermometry Results.- To showcase the broad applicability of these techniques, we consider a different setup for the thermometry case: a detector motivated by a superconducting circuit undergoing a long-range interaction with an open transmission line. A physically motivated UV-cutoff for such systems can be given by $K = 50$ GHz/c [42, 47, 48]. This gives a lattice spacing of $a = \pi/K = 1.8$ cm. If the circuit couples to the transmission line with a Gaussian profile and we take this cutoff to be at $K = 7/\sigma$, this suggests that the circuit couples to the transmission line over a lengthscale $\sigma = 4.2$ cm, a reasonable value [42]. We take the circuit to be coupled to the center of a transmission line box with size $L = 100a = 44.8\sigma = 188$ cm. Further, we take the circuit to have an energy gap typical of such systems, $\omega_D = 10$ GHz and the field to have a mass $mc^2/\hbar = 0.1$ GHz, much smaller than the other energy scales. We again consider the strong coupling regime, where $\lambda_0/\hbar = \omega_D = 10$ GHz. We would like to know if the local probe can determine the temperature of the

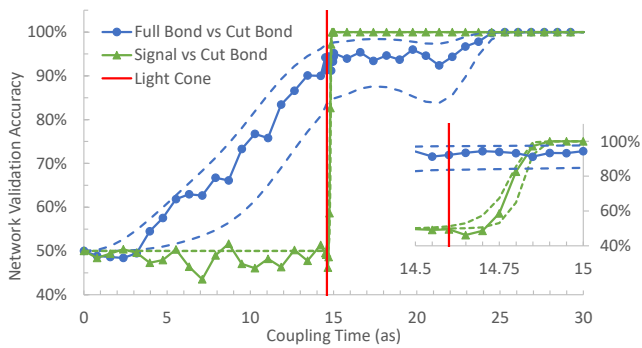


FIG. 1. We trained a neural network to predict the boundary condition of a quantum field from local probe data gathered far from the boundary. The network was asked a) to detect a signal sent from the boundary (green triangles) and b) to detect a modification of the field’s boundary condition (blue circles). The network’s accuracy (solid) along with upper and lower bounds on the theoretical optimal accuracy (dashed) are plotted as a function of the duration of the probe’s interaction with the field. A point plotted at time t indicates the network’s accuracy given measurements taken at $N_{\text{TIMES}} = 10$ measurement times between t and the previous plot point. The network was trained on $n_{\text{train}} = 1500$ examples. Each example summarizes $N_{\text{TOM}} = 10^{20}$ measurements of each of the probe’s quadratures (\hat{q}_D , \hat{r}_D and \hat{p}_D) at each measurement times. The inset shows details of the causal response to the detector to the signal. The vertical red line is at the edge-of-detector-to-boundary light-crossing time.

field in the transmission line with an accuracy of $\pm 1\%$. This is typically challenging because the temperatures of such systems are usually of the order of mK [48]. For our toy example, we are asking the neural network to classify the states of the field in eleven boxes with a width of $\pm 1\%$ around a temperature scale T . In other words, the network classifies the measurement data in boxes of width $0.02T$ from $[0.89T, 0.91T]$ to $[1.09T, 1.11T]$.

As Fig 2 shows, with $N_{\text{tom}} = 10^{10}$, the neural network can determine the temperature very accurately even for very low transmission line temperature (sub-mK). Notice, that the network can extract the temperature of the field even in cases where the detector is interacting with the field for times that are shorter than the thermalization scales of the problem, in fact faster than the detector’s Heisenberg time $1/\omega_D = 100$ ps (which lower-bounds thermalization time). The computational complexity of adding additional boxes—keeping similar accuracy—scales favourably. The neural network can also be easily trained to do a best estimate of the temperature (through regression [45]) rather than binning. We have not included this here to keep the parallelism with the boundary determination case, but the efficiency of the network in such a task is similar.

Conclusions.- We proposed the use of machine learning techniques in quantum field theory to regather information scrambled in space and time. We have shown how to read out non-local features of a QFT from the outcome

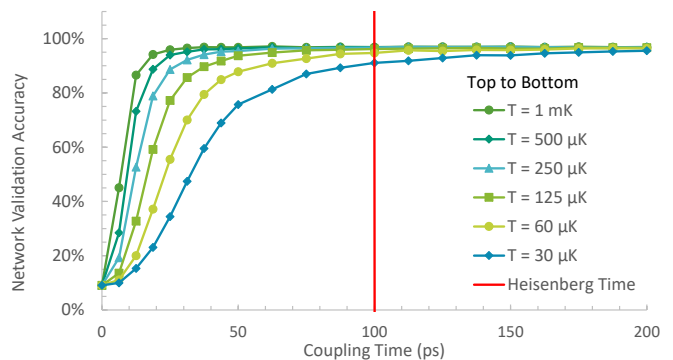


FIG. 2. A neural network trained to predict the temperature of a quantum field to an accuracy of 1% from local probe data. The network assigns the field temperature to one of eleven bins each with width of $0.02T$: from $[0.89T, 0.91T]$ to $[1.09T, 1.11T]$. The network’s accuracy is plotted as function of the duration of the probe’s interaction with the field. A point plotted at time t indicates the network’s accuracy given measurements taken at $N_{\text{TIMES}} = 10$ measurement times between t and the previous plot point. The network was trained on $n_{\text{train}} = 3750$ examples from each range. Each example summarizes $N_{\text{TOM}} = 10^{10}$ measurements of each of the probe’s quadratures (\hat{q}_D , \hat{r}_D and \hat{p}_D) at each measurement time. The vertical red line is the probe’s Heisenberg time ω_D^{-1} .

of local experiments, processed through a neural network. In particular we have shown how a local probe can see a wall far away from it, in the vacuum and without actively sending signals to bounce off it. We have also shown how a local probe that is not given enough time to thermalize can accurately determine the temperature of a quantum field.

With this, we showed how statistical processing of local measurements and machine learning algorithms can extract and unscramble non-local information that (via thermalization [15–20]) the field scrambled over a large region of spacetime. The measurement protocol that we considered is very simple and not adapted to the particular toy problems considered in this letter, and yet we were able to distinguish with almost certainty the relevant features of the field we were after. This showcases the potential of these methods to accommodate experimental needs. Namely, the use of machine learning techniques in the context of quantum field theory takes the complexity burden out of the choice of the concrete experimental implementations (measurement variables and protocols) and puts it on the data processing, which neural networks can deal with efficiently.

While these examples are relatively simple, the techniques we present in this letter are general and of wide applicability. This paves the way to the use of machine learning techniques in more complicated scenarios such as distinguishing gravitational backgrounds [12, 49], global state tomography [25] with local probes, acknowledging entanglement in analog Hawking radiation [50], and even new experimental proposals seeking direct evidence of untested QFT phenomena such as the Unruh

effect [37]. Finally, the techniques developed here are directly translatable to their use in many-body quantum physics, where they can be used to address the problem of measuring many-body observables with local probes in, e.g., quantum phase transitions [51].

ACKNOWLEDGMENTS

EMM acknowledges support through the Discovery Grant Program of the Natural Sciences and Engineering Research Council of Canada (NSERC). EMM also acknowledges support of his Ontario Early Researcher award. DG acknowledges support by NSERC through a Vanier Scholarship. This work was made possible by the facilities of the Shared Hierarchical Academic Research Computing Network (SHARC-NET:www.sharcnet.ca) and Compute/Calcul Canada.

Appendix A: Free scalar QFT on the lattice

As we discussed in the main text, we can motivate a UV cutoff for the field-probe system through the length scale of probe's smearing function. To see this, let us expand the field-probe interaction Hamiltonian

$$\hat{\mathcal{H}}_{\text{INT}} = \lambda \chi(t) \int_{-\infty}^{\infty} dx F(x) \hat{q}_{\text{D}} \otimes \hat{\phi}(x). \quad (\text{A1})$$

in terms of plane-wave modes as

$$\hat{\mathcal{H}}_{\text{INT}} = \lambda \chi(t) \hat{q}_{\text{D}} \int_{\mathbb{R}^2} \frac{dx dk}{2\sqrt{\pi\omega_k}} F(x) (e^{-i\omega_k t} e^{ikx} \hat{a}_k + \text{H.c.}) = \lambda \chi(t) \hat{q}_{\text{D}} \int_{-\infty}^{\infty} \frac{dk}{2\sqrt{\pi\omega_k}} \left(\tilde{F}(k) e^{-i\omega_k t} \hat{a}_k + \text{H.c.} \right),$$

where $\tilde{F}(k) = \mathcal{F}_k[F(x)]$ is the Fourier transform of $F(x)$. Note that $\tilde{F}(k)$ determines how strongly the probe couples to each of the field modes. If the smearing function is strongly supported only on a finite region of size $\sim \sigma$ (e.g., $F(x)$ is a Gaussian with standard deviation σ) then $\tilde{F}(k)$ would have a width $\sim 1/\sigma$. That is, the probe would not couple strongly to modes with wavenumber $|k| \gg \sigma^{-1}$. Thus by considering a probe with a finite spatial extent we are automatically considering a soft-UV cutoff in the interaction of field and probe.

If $\tilde{F}(k)$ decays sufficiently fast, we may be justified in dropping the coupling to the modes above some large UV threshold, say $|k| > K$ (e.g. for a Gaussian profile we can take $K = 7/\sigma$). Cutting off the UV like this yields an effective coupling of $\tilde{F}^{\text{UV}}(k) := \Pi_K(k)\tilde{F}(k)$ where $\Pi_K(k)$ is the rectangle function over $k \in [-K, K]$. By the Nyquist Shannon sampling theorem we can then reconstruct our UV cutoff smearing function, $F^{\text{UV}}(x) := \mathcal{F}^{-1}[\tilde{F}^{\text{UV}}(k)]$, as $F^{\text{UV}}(x) = \sum_n F(x_n) S_n(x/a)$, where $a = \pi/K$ is the spacing of the discrete positions, $x_n = na$, and where $S_n(r) := \sin(\pi(r-n))/\pi(r-n)$ is a displaced normalized sinc function. Note that while $S_n(r)$ decays only polynomially for large r , our reconstructed smearing may still effectively decay exponentially. For instance, in our Gaussian smearing example, the reconstruction exactly matches the original (exponentially suppressed) smearing function at each discrete point x_n .

We hence define the UV-cutoff interaction Hamiltonian as

$$\hat{\mathcal{H}}_{\text{INT}}^{\text{UV}} := \lambda \chi(t) \int_{-\infty}^{\infty} dx F^{\text{UV}}(x) \hat{q}_{\text{D}} \otimes \hat{\phi}(x) = \lambda \chi(t) \int_{-\infty}^{\infty} dx F^{\text{UV}}(x) \hat{q}_{\text{D}} \otimes \hat{\phi}^{\text{UV}}(x) \quad (\text{A2})$$

where we note that the UV cutoff smearing function effectively induces a UV cutoff of the field operator, $\hat{\phi}^{\text{UV}}(x) := \mathcal{F}_x^{-1}[\Pi_K(k)\mathcal{F}_k[\hat{\phi}(x)]]$. Next, we note that since $\hat{\phi}^{\text{UV}}(x)$ is bandlimited we can express it as a sum of sinc functions as, $\hat{\phi}^{\text{UV}}(x) = \sum_n \hat{\phi}(x_n) S_n(x/a)$ where $x_n := (t, x_n)$. Recomputing the UV cutoff interaction Hamiltonian using these sinc representations we find

$$\hat{\mathcal{H}}_{\text{INT}}^{\text{UV}} = \lambda \chi(t) \sum_n a F(x_n) \hat{q}_{\text{D}} \otimes \hat{\phi}(x_n) \quad (\text{A3})$$

where we have used the orthonormality of the collection $\{S_m(r)\}$ in the L^2 norm. Thus, by taking a hard UV cutoff on the probe's smearing function we automatically find that the probe effectively only couples to the field at the discrete positions, $x_n = na$.

Notice that so far, we are not implying that the field itself has a UV cutoff or that the space it lives on is discretized. We have only discussed an approximation of the probe coupling. We could study the field theory as is without an

explicit UV cutoff, but for our purposes it is convenient to consider that the field is also UV-cutoff. We apply this UV-cutoff to the field by removing the field modes with $k > |K|$ by defining the UV cutoff field operators,

$$\hat{\phi}^{\text{UV}}(\mathbf{x}) := \mathcal{F}_x^{-1} [\Pi_K(k) \mathcal{F}_k[\phi(\mathbf{x})]], \quad \hat{\pi}^{\text{UV}}(\mathbf{x}) := \mathcal{F}_x^{-1} [\Pi_K(k) \mathcal{F}_k[\pi(\mathbf{x})]], \quad \partial_x \hat{\phi}^{\text{UV}}(\mathbf{x}) := \mathcal{F}_x^{-1} [\Pi_K(k) \mathcal{F}_k[\partial_x \phi(\mathbf{x})]], \quad (\text{A4})$$

where where $\mathbf{x} := (t, x)$. Note that since these operators are now band limited we can express them as sums of sinc functions as,

$$\hat{\phi}^{\text{UV}}(\mathbf{x}) = \sum_n \hat{\phi}(x_n) S_n(x/a), \quad \hat{\pi}^{\text{UV}}(\mathbf{x}) = \sum_n \hat{\pi}(x_n) S_n(x/a), \quad \partial_x \hat{\phi}^{\text{UV}}(\mathbf{x}) = \sum_n \partial_x \hat{\phi}(x_n) S_n(x/a). \quad (\text{A5})$$

Using these UV cutoff operators we define the UV cutoff field Hamiltonian as,

$$\hat{\mathcal{H}}_\phi^{\text{UV}} := \frac{1}{2} \int_{-\infty}^{\infty} dx \, c^2 \hat{\pi}^{\text{UV}}(\mathbf{x})^2 + (\partial_x \hat{\phi}^{\text{UV}}(\mathbf{x}))^2 + \frac{m^2 c^2}{\hbar^2} \hat{\phi}^{\text{UV}}(\mathbf{x})^2 = \frac{a}{2} \sum_n c^2 \hat{\pi}(x_n)^2 + (\partial_x \hat{\phi}(x_n))^2 + \frac{m^2 c^2}{\hbar^2} \hat{\phi}(x_n)^2 \quad (\text{A6})$$

where we have again used the operator's sinc representations and L^2 orthonormality of $\{S_m(r)\}$ to express the integral as a sum. Next, taking the discrete approximation for the derivative, $\partial_x \hat{\phi}(x_n) \approx [\hat{\phi}(x_{n+1}) - \hat{\phi}(x_n)]/a$, we find,

$$\hat{\mathcal{H}}_\phi^{\text{UV}} \approx \frac{a}{2} \sum_n c^2 \hat{\pi}^2(x_n) + \left(\frac{\hat{\phi}(x_{n+1}) - \hat{\phi}(x_n)}{a} \right)^2 + \frac{m^2 c^2}{\hbar^2} \hat{\phi}^2(x_n). \quad (\text{A7})$$

We note that these satisfy the commutation relations, $[\hat{\phi}(x_n), \hat{\pi}(x_m)] = i\hbar(\delta_{nm}/a)\mathbb{1}$. Finally, rewriting this Hamiltonian in terms of the dimensionless operators, $\hat{q}_n = \sqrt{am/\hbar^2} \hat{\phi}(x_n)$ and $\hat{p}_n = \sqrt{a/m} \hat{\pi}(x_n)$ which satisfy the commutation relations, $[\hat{q}_i, \hat{p}_j] = i\delta_{ij}\mathbb{1}$, yields the UV cutoff field Hamiltonian claimed in the main text.

Appendix B: Preprocessing, Neural Network Architecture and Training Details

As we discussed in the main text, the data from each run of our measurement procedure can be losslessly compressed to a vector, $\mathbf{x} \in \mathbb{R}^d$ where $d = 6N_{\text{TIMES}}$ and associated with a label y denoting which boundary condition or temperature the field had. We can collect n instances of this data into a $d \times n$ design matrix $\mathbf{X} = (\mathbf{x}_1, \dots, \mathbf{x}_n)^\top$ and a vector of labels $\mathbf{y} = (y_1, \dots, y_n)^\top$. We then portion off 75% of this data ($n_{\text{train}} = 0.75n$) to be used for training the neural network $\mathbf{X}_{\text{train}}$ and $\mathbf{y}_{\text{train}}$ leaving the other 25% ($n_{\text{valid}} = 0.25n$) as validating data, $\mathbf{X}_{\text{valid}}$ and $\mathbf{y}_{\text{valid}}$ which we will ultimately use to test the accuracy of the trained network. Note that the network will not be exposed to any of the validation data during training.

We begin processing our data by subtracting off the mean of the training data, $\mathbf{X} \rightarrow \mathbf{X} - \mathbf{X}_{\text{train}}^{\text{avg}}$, where $\mathbf{X}_{\text{train}}^{\text{avg}} = \sum_{k=1}^{n_{\text{train}}} \mathbf{x}_k / n_{\text{train}}$. Next we do principle component analysis (PCA) which finds a representation of our data without linear correlations. To do this we compute the covariance matrix of our training data and perform a singular value decomposition on it,

$$\frac{1}{n_{\text{train}} - 1} \mathbf{X}_{\text{train}}^\top \mathbf{X}_{\text{train}} = \sum_{j=1}^d \lambda_j \boldsymbol{\xi}_j \boldsymbol{\xi}_j^\top. \quad (\text{B1})$$

The singular vectors, $\boldsymbol{\xi}_j$, are the directions in our data $\mathbf{X}_{\text{train}}$ varies independently. The singular values, $\lambda_j \in \mathbb{R}$, indicate ‘‘how much’’ variance is in each direction. Using this decomposition we can rewrite our data as $\mathbf{X} \rightarrow U\mathbf{X}$ where $U = (\boldsymbol{\xi}_1, \dots, \boldsymbol{\xi}_d)^\top$. In this basis, the training data has a diagonal covariance matrix. Finally we can whiten the data as $\mathbf{X} \rightarrow \Lambda^{-1/2} \mathbf{X}$ where $\Lambda = \text{diag}(\lambda_0, \dots, \lambda_{2d})$. The covariance matrix of the training data is now the identity matrix.

The data is now ready to begin training the neural network. Neural Networks work by alternately applying tuneable linear-affine transformations (controlled by weights and biases) and fixed non-linear transformations (the activator function) to their inputs. See Fig. 3 for a schematic of a neural network can be used to classifying the QFTs based on local probe measurement data.

The data to be classified is first input on the left-most layer of the network. The data then passes rightward through the network, undergoing tuneable linear-affine transformations (represented by lines) between each layer and fixed non-linear transformations across each layer (represented by circles).

For our applications, we use a network with three layers, 60 neurons on the input layer, 30 in the intermediate (hidden) layer, and 2 or 11 neurons in the final layer depending on how many classes we are trying to differentiate.

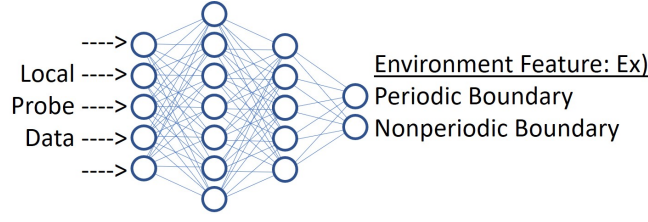


FIG. 3. (Color online.) A schematic of a neural network for processing local probe data to learn about features of a QFT.

The network is fully connected with a leaky rectified linear units as our activator function. In the final layer where we use a soft max function to ensure the output is a probability. Given some weights, W , and biases, b , we evaluated the networks performance by the cross-entropy cost function

$$C(W, b) = \frac{-1}{n_{\text{train}}} \sum_{k=1}^{n_{\text{train}}} \tilde{y}_k \cdot \log(f(\mathbf{x}_k; W, b)) \quad (\text{B2})$$

where \tilde{y}_k is the one-hot encoding of the k^{th} data point's label and $f(\mathbf{x}_k; W, b)$ is the neural networks predicted probabilities for the label of data point \mathbf{x}_k .

To help reduce overfitting we add an L_2 regularizer to this cost function, $\sim \lambda_2 \|W\|_2$. This penalizes the network for using large weights. Additionally when training the network we randomly “drop” some fraction of the neurons. This forces the network to be more robust. The sum of the cost function and the regularizer are then minimized by stochastic gradient descent.

Appendix C: Total Variation and Hellinger Distances for Binary Boundary Classification

Consider the binary classification problem where we are asked to pick a label $y = 0$ or $y = 1$ for data \mathbf{x}_0 drawn from either $r_\theta(\mathbf{x}) = p(\mathbf{x}|y = 0, \theta)$ or from $q_\theta(\mathbf{x}) = p(\mathbf{x}|y = 1, \theta)$ with equal odds, where θ is some free parameter of the problem. In terms of the scenarios considered in the main text, \mathbf{x} is the local probe data, y labels the either field's boundary conditions or a temperature range and θ describes the other details of the scenario, for instance the probe's coupling time. The distributions $r_\theta(\mathbf{x})$ and $q_\theta(\mathbf{x})$ are then the odds that some particular data was produced given some field and measurement procedure.

The optimal strategy (i.e., the one which maximizes your success probability) for this binary classification problem is to guess $y = 1$ if $q_\theta(\mathbf{x}) > r_\theta(\mathbf{x})$ and $y = 0$ if $r_\theta(\mathbf{x}) > q_\theta(\mathbf{x})$, breaking ties randomly. This strategy succeeds with probability of $p_{\text{success}} = \frac{1}{2}(1 + \text{TV}(p, q))$ where

$$\text{TV}(r_\theta, q_\theta) = \frac{1}{2} \int |r_\theta(\mathbf{x}) - q_\theta(\mathbf{x})| d\mathbf{x}. \quad (\text{C1})$$

is the total variation distance between $r_\theta(\mathbf{x})$ and $q_\theta(\mathbf{x})$. If we can compute this distance, we can determine for which values of θ (e.g., for which coupling times) the distributions $r_\theta(\mathbf{x})$ and $q_\theta(\mathbf{x})$ are distinguishable.

The total variation distance is only useful for binary problems (such as our first toy example). It cannot be used for more complex scenarios such as our thermometry example. Even for the boundary distinction scenario considered in the main text, calculating the total variation distance directly is infeasible. An alternate approach that will work for one of the scenarios is to compute upper and lower bounds using the Hellinger distance, $H(r, q)$ [52], as

$$H(r_\theta, q_\theta)^2 \leq \text{TV}(r_\theta, q_\theta) \leq H(r_\theta, q_\theta) \sqrt{2 - H(r_\theta, q_\theta)^2} \quad \text{where} \quad H(r, q) = \frac{1}{\sqrt{2}} \sqrt{\int (\sqrt{r(\mathbf{x})} - \sqrt{q(\mathbf{x})})^2 d\mathbf{x}} \quad (\text{C2})$$

Unfortunately, for the distributions arising in the main text, the Hellinger distance is no easier to compute. However, in the high tomography regime ($N_{\text{TOM}} \gg 1$) we can apply the central limit theorem to approximate r_θ and q_θ by multivariate normal distribution, $r_\theta(\mathbf{x}) = \mathcal{N}(\mathbf{x}; \mu_r, \Sigma_r)$ and $q_\theta(\mathbf{x}) = \mathcal{N}(\mathbf{x}; \mu_q, \Sigma_q)$ for some means, μ_r and μ_q , and some covariances, Σ_q and Σ_r . The Hellinger distance between two such multivariate normal distributions is [52]

$$H(r_\theta, q_\theta)^2 = 1 - \left(\frac{\det(\Sigma_r \Sigma_q)}{\det(\bar{\Sigma}^2)} \right)^{\frac{1}{4}} \exp \left(-\frac{\Delta\mu^\top \bar{\Sigma}^{-1} \Delta\mu}{8} \right). \quad (\text{C3})$$

where $\Delta\mu = \mu_r - \mu_q$ and $\bar{\Sigma} = (\Sigma_r + \Sigma_q)/2$. Thus if we can compute the means and covariances of our data, we can find bounds for the neural network's optimal performance.

Recall that due to the Gaussian nature of our setup all of our measurement results were drawn from normal distributions. Moreover as we discussed in the main text, all of these measurements are independent, and many are identically distributed. Thus we needed only record the sample means and variances of each quadrature at each time point. For clarity we will restrict our discussion to the our N_{TOM} measurements of \hat{q} at $t = \Delta t$. From these measurements we need only record

$$\bar{q} = \frac{1}{N_{\text{TOM}}} \sum_{k=1}^{N_{\text{TOM}}} q_k, \sim \mathcal{N}\left(\langle \hat{q} \rangle, \frac{\sigma_{qq}}{N_{\text{TOM}}}\right), \quad \text{and} \quad \bar{s}_q^2 = \frac{1}{N_{\text{TOM}} - 1} \sum_{k=1}^{N_{\text{TOM}}} (q_k - \bar{q})^2 \sim \sigma_{qq} \frac{\chi^2(N_{\text{TOM}} - 1)}{N_{\text{TOM}} - 1}, \quad (\text{C4})$$

where $\chi^2(k)$ is the chi-squared distribution with k degrees of freedom [53] and $\langle \hat{q} \rangle$ and $\sigma_{qq} = \langle \hat{q}^2 \rangle - \langle \hat{q} \rangle^2$ are the probe's first and second moments in \hat{q} at $t = \Delta t$. Due to the Gaussian nature of our setup, these moments can be efficiently computed from a fixed initial condition. This allows us to efficiently compute the distribution of our compressed data at least in the boundary condition classification case. In the temperature classification problem, however, these moments depend on the initial temperature which is itself treated as a random variable. Thus in this case the final distribution of our compressed data is a compound probability distribution which is much more difficult to analyze.

Continuing our analysis of the boundary condition classification scenario, for large N_{TOM} , we can apply the central limit theorem yielding

$$\bar{q} \sim \mathcal{N}\left(\langle \hat{q} \rangle, \frac{\sigma_{qq}}{N_{\text{TOM}}}\right), \quad \text{and} \quad \bar{s}_q^2 \sim \mathcal{N}\left(\sigma_{qq}, \frac{2\sigma_{qq}^2}{N_{\text{TOM}} - 1}\right) \quad (\text{C5})$$

Thus in the high tomography regime, our compressed data,

$$\mathbf{x} = (\bar{q}(t), \bar{r}(t), \bar{p}(t), \bar{s}_q^2(t), \bar{s}_r^2(t), \bar{s}_p^2(t) \quad \text{for } t = \Delta t, 2\Delta t, \dots, T_{\text{MAX}}) \quad (\text{C6})$$

is distributed as $\mathbf{x} \sim \mathcal{N}(\mu, \Sigma)$ where

$$\boldsymbol{\mu} = (\langle \hat{q}(t) \rangle, \langle \hat{r}(t) \rangle, \langle \hat{p}(t) \rangle, \sigma_{qq}(t), \sigma_{rr}(t), \sigma_{pp}(t) \quad \text{for } t = \Delta t, 2\Delta t, \dots, T_{\text{MAX}}) \quad (\text{C7})$$

$$\Sigma = \frac{1}{N_{\text{TOM}}} \text{diag}(\sigma_{qq}(t), \sigma_{rr}(t), \sigma_{pp}(t), 2\sigma_{qq}^2(t), 2\sigma_{rr}^2(t), 2\sigma_{pp}^2(t) \quad \text{for } t = \Delta t, 2\Delta t, \dots, T_{\text{MAX}}). \quad (\text{C8})$$

Knowing this distribution we can compute the Hellinger distance and place bounds on optimal classification rate.

- [1] M. Redhead, *Foundations of Physics* **25**, 123 (1995).
- [2] A. Ortega, E. McKay, A. M. Alhambra, and E. Martín-Martínez, *Phys. Rev. Lett.* **122**, 240604 (2019).
- [3] R. D. Sorkin, "Impossible measurements on quantum fields," (1993), arXiv:gr-qc/9302018 [gr-qc].
- [4] F. Dowker, "Useless qubits in "relativistic quantum information"," (2011), arXiv:1111.2308 [quant-ph].
- [5] D. M. T. Benincasa, L. Borsten, M. Buck, and F. Dowker, *Class. Quantum Gravity* **31**, 075007 (2014).
- [6] E. Martín-Martínez and P. Rodríguez-Lopez, *Phys. Rev. D* **97**, 105026 (2018).
- [7] C. J. Fewster and R. Verch, "Quantum fields and local measurements," (2018), arXiv:1810.06512 [math-ph].
- [8] E. Martín-Martínez and P. Rodríguez-Lopez, *Phys. Rev. D* **97**, 105026 (2018).
- [9] S. Takagi, *Prog. Theor. Phys. Supp.* **88**, 1 (1986).
- [10] L. Hodgkinson and J. Louko, *Phys. Rev. D* **86**, 064031 (2012).
- [11] A. Ahmadzadegan, E. Martín-Martínez, and R. B. Mann, *Phys. Rev. D* **89**, 024013 (2014).
- [12] A. R. H. Smith and R. B. Mann, *Classical and Quantum Gravity* **31**, 082001 (2014).
- [13] K. K. Ng, R. B. Mann, and E. Martín-Martínez, *Phys. Rev. D* **96**, 085004 (2017).
- [14] A. Ahmadzadegan, F. Lalegani, and R. B. Mann, "Seeing in complete darkness, using the unruh effect," (2019), arXiv:1902.06745.
- [15] D. N. Page, *Phys. Rev. Lett.* **71**, 3743 (1993).
- [16] E. Martín-Martínez, A. R. H. Smith, and D. R. Terno, *Phys. Rev. D* **93**, 044001 (2016).
- [17] J. Maldacena, S. H. Shenker, and D. Stanford, *J. High Energy Phys.* **2016**, 106 (2016).
- [18] B. Yoshida and A. Kitaev, "Efficient decoding for the Hayden-Preskill protocol," (2017), arXiv:1710.03363.
- [19] K. A. Landsman, C. Figgatt, T. Schuster, N. M. Linke, B. Yoshida, N. Y. Yao, and C. Monroe, *Nature* **567**, 61 (2019).
- [20] K. Yamaguchi, N. Watamura, and M. Hotta, *Phys. Lett. A* **383**, 1255 (2019).
- [21] A. Hentschel and B. C. Sanders, *Phys. Rev. Lett.* **107**, 233601 (2011).
- [22] C. E. Granade, C. Ferrie, N. Wiebe, and D. G. Cory, *New J. Phys* **14**, 103013 (2012).

- [23] J. Carrasquilla and R. G. Melko, *Nat. Phys.* **13**, 431 (2017).
- [24] Y. Quek, S. Fort, and H. Khoo Ng, arXiv e-prints, arXiv:1812.06693 (2018), arXiv:1812.06693 [quant-ph].
- [25] G. Torlai, G. Mazzola, J. Carrasquilla, M. Troyer, R. Melko, and G. Carleo, *Nat. Phys.* **14**, 447 (2018).
- [26] E. S. Tiunov, V. V. Tiunova, A. E. Ulanov, A. I. Lvovsky, and A. K. Fedorov, arXiv e-prints, arXiv:1907.06589 (2019), arXiv:1907.06589 [quant-ph].
- [27] K. Zhou, G. Endrődi, L.-G. Pang, and H. Stöcker, *Phys. Rev. D* **100**, 011501 (2019).
- [28] P. E. Shanahan, D. Trewartha, and W. Detmold, *Phys. Rev. D* **97**, 094506 (2018).
- [29] Y. Mori, K. Kashiwa, and A. Ohnishi, *Prog. Theor. Exp. Phys.* **2018** (2018), 10.1093.
- [30] W. G. Unruh and W. H. Zurek, *Phys. Rev. D* **40**, 1071 (1989).
- [31] B. L. Hu and A. Matacz, *Phys. Rev. D* **49**, 6612 (1994).
- [32] S. Massar and P. Spindel, *Phys. Rev. D* **74**, 085031 (2006).
- [33] S.-Y. Lin and B. L. Hu, *Phys. Rev. D* **76**, 064008 (2007).
- [34] E. Martín-Martínez, I. Fuentes, and R. B. Mann, *Phys. Rev. Lett.* **107**, 131301 (2011).
- [35] N. Friis, M. Huber, I. Fuentes, and D. E. Bruschi, *Phys. Rev. D* **86**, 105003 (2012).
- [36] E. G. Brown, E. Martín-Martínez, N. C. Menicucci, and R. B. Mann, *Phys. Rev. D* **87**, 084062 (2013).
- [37] W. G. Unruh, *Phys. Rev. D* **14**, 870 (1976).
- [38] B. DeWitt, in *General Relativity: an Einstein Centenary Survey*, edited by Hawking, S. and Israel, W. (Cambridge University Press, Cambridge, 1979).
- [39] A. Pozas-Kerstjens and E. Martín-Martínez, *Phys. Rev. D* **94**, 064074 (2016).
- [40] J. B. Kogut, *Rev. Mod. Phys.* **51**, 659 (1979).
- [41] C. Gattringer and C. B. Lang, *Lect. Notes Phys.* **788**, 1 (2010).
- [42] E. McKay, A. Lupascu, and E. Martín-Martínez, *Phys. Rev. A* **96**, 052325 (2017).
- [43] B. L. Schumaker, *Phys. Rep.* **135**, 317 (1986).
- [44] R. A. Fisher, *Philos. Trans. Royal Soc. A* **222**, 309 (1922).
- [45] I. Goodfellow, Y. Bengio, and A. Courville, *Deep Learning* (MIT Press, Cambridge, US, 2016) <http://www.deeplearningbook.org>.
- [46] D. Grimmer, I. Melgarejo-Lermas, and E. Martín-Martínez, <https://github.com/BarrioRQI/MachineLearningQFT> (2019).
- [47] D. H. Douglass and R. Meservey, *Phys. Rev.* **135**, A19 (1964).
- [48] P. Forn-Díaz, J. J. García-Ripoll, B. Peropadre, J.-L. Orgiazzi, M. A. Yurtalan, R. Belyansky, C. M. Wilson, and A. Lupascu, *Nat. Phys.* **13**, 39 (2016).
- [49] K. K. Ng, R. B. Mann, and E. Martín-Martínez, *Phys. Rev. D* **94**, 104041 (2016).
- [50] J. Steinhauer, *Nat. Phys.* **12**, 959 (2016).
- [51] Z. Xu and A. del Campo, *Phys. Rev. Lett.* **122**, 160602 (2019).
- [52] A. Bhattacharyya, *Sankhya* **7**, 401 (1946).
- [53] W. G. Cochran, *Mathematical Proceedings of the Cambridge Philosophical Society* **30**, 178191 (1934).